



On the onset of instability in the wake of super-hydrophobic spheres

Marco Castagna, Nicolas Mazellier, Azeddine Kourta

► To cite this version:

Marco Castagna, Nicolas Mazellier, Azeddine Kourta. On the onset of instability in the wake of super-hydrophobic spheres. International Journal of Heat and Fluid Flow, 2021, 87, pp.108709. 10.1016/j.ijheatfluidflow.2020.108709 . hal-03280224

HAL Id: hal-03280224

<https://hal.science/hal-03280224>

Submitted on 15 Dec 2022

HAL is a multi-disciplinary open access archive for the deposit and dissemination of scientific research documents, whether they are published or not. The documents may come from teaching and research institutions in France or abroad, or from public or private research centers.

L'archive ouverte pluridisciplinaire **HAL**, est destinée au dépôt et à la diffusion de documents scientifiques de niveau recherche, publiés ou non, émanant des établissements d'enseignement et de recherche français ou étrangers, des laboratoires publics ou privés.



Distributed under a Creative Commons Attribution - NonCommercial 4.0 International License

On the onset of instability in the wake of super-hydrophobic spheres

Marco Castagna^a, Nicolas Mazellier^{a,*}, Azeddine Kourta^a

^a *University of Orléans, INSA-CVL, PRISME, EA 4229, 45072 Orléans, France*

Abstract

We report an experimental investigation of free falling super-hydrophobic (SH) spheres in glycerine-water mixtures over a wide range of Reynolds number. SH coatings have the ability to reduce the contact area between the surrounding liquid and the solid surface by entrapping an air layer in the surface roughness. We investigate the effect of this air plastron on the hydrodynamic performance of spheres, focusing our attention on the onset of wake instabilities. Our results emphasise the key role of the surface roughness properties on the triggering of wake instabilities. It is shown that, unlike what was reported in previous numerical studies on SH bluff-bodies, local deformation of the interface may act as a by-pass mechanism promoting earlier transition, yielding a decrease of the critical Reynolds number at which the wake becomes unstable. A scenario coupling the hydrodynamic instabilities (scaling with the Reynolds number) and the interface deformation (scaling with the roughness-based Weber number) is proposed to describe the different transition mechanisms in presence of SH surfaces. It is found that the promotion of wake instabilities over SH surfaces occurs when the roughness-based Weber number is larger than a critical threshold. These findings are of primary importance for guiding the design of resilient and efficient SH surfaces.

Keywords: super-hydrophobic surfaces, wake, transition, Weber number,

*Corresponding author

Email addresses: marco_castagna@outlook.com (Marco Castagna),
nicolas.mazellier@univ-orleans.fr (Nicolas Mazellier),
azeddine.kourta@univ-orleans.fr (Azeddine Kourta)

1. Introduction

The presence of an air layer between a solid surface and a liquid interacting with it may be interesting for a large range of industrial applications, encompassing glasses for self-cleaning windows, retarding ice-growth rate surfaces, corrosion-resistant equipments and drag-reducing walls for liquids transport or moving objects [1]. Among the various methods developed to achieve this lubricating effect, the fast growth of super-hydrophobic (SH) coatings emphasises the attractiveness of this kind of surface as a mean to control, in a passive manner, the hydrodynamics of marine vehicles. While a number of studies have been conducted to investigate the effect of SH surfaces in laminar and turbulent regimes, few works have been devoted to their performance in transitional conditions. [2] numerically analysed the stability and the transition to turbulence of a channel flow in presence of SH walls modelled by a homogeneous slip condition. They showed a significant impact on the critical Reynolds number at which instability appears. More recently, [3] went one step further by investigating the transition mechanisms in a channel flow via Direct Numerical Simulations. The SH surfaces influence was found to be extremely sensitive to the type of perturbation used to excite the baseline flow. For modal (linear) disturbances, slippery conditions delay the onset of turbulence, whereas they become ineffective to modify transition for non-modal disturbances. For what concerns the influence of SH surfaces on the flow over bluff-bodies, [4] and [5] numerically investigated the wake dynamics at low Reynolds number of a two-dimensional (2D) circular cylinder and a D-shaped body, respectively. Very recently, the wake of a SH circular cylinder over a broad range of Reynolds number was investigated experimentally by [6]. All in all, these studies emphasised that instability modes are strongly impacted by the SH surfaces. However, these analyses were based on the assumption that the shape of the air-liquid interface is flat and time independent.

Recent experimental works revealed that the non-deformable assumption could be too simplistic to correctly (or fully) describe the SH coatings behaviour. Moreover, under certain operating conditions, the deformation of the air-liquid interface may induce strong effects on the flow and its associated loads. For instance, [7] showed that the flow profile in the proximity of the air-liquid interface was influenced by the shape of the latter (i.e. concave or convex), thus affecting the magnitude of the beneficial slip. The role played by the air-liquid interface shape on the pressure drop induced by a laminar flow through a peculiar array of apple-shaped pillars was investigated by [8] in a micro-channel configuration. These authors found that the skin friction reduction due to the presence of the air-water interface could be mitigated, if not exceeded, by the form drag increase induced by the shape of the interface. The interface deformation effect was also investigated by [9] who analysed the trajectory of SH spheres falling in a water tank. They observed that the loads experienced by the sphere at terminal conditions are strongly dependent on the interface shape. They introduced a critical aspect ratio to distinguish between the beneficial and the unfavorable influence of SH coatings on drag. This detrimental effect was also observed in numerical simulations of turbulent channel flows in presence of SH walls. Pressure fluctuations in the wall proximity were found by [10], and later on by [11], to be affected by the air-liquid interface deformation, which was described by a linearised Young-Laplace approach. The authors thus suggested an influence on the robustness of SH surfaces in realistic turbulent conditions. Similarly, the tracking method used by [12] to describe the temporal evolution of the air-liquid interface shape highlighted a possible detrimental effect on SH surfaces drag reduction ability, when compared to an ideal flat interface. [13] investigated the influence of interface deformation on the transition in a channel flow. Even for interface motion much smaller than the typical surface texture size, [13] showed that the transition to turbulence is triggered much earlier compared to steady interfaces. In particular, [13] reported that the interface movement is synchronized with the passage of coherent structures, which induces ejection events promoting the creation of hairpin heads which subsequently breakdown

to turbulence.

The key parameter emphasised by these cited studies is the Weber number, which reflects the capability of the interface to deform under the action of flow perturbations. This parameter could be written in a general form as $We = \rho u^2 \ell / \gamma$, where ρ and γ denote the liquid density and the liquid-gas surface tension, respectively, while u and ℓ represent typical velocity and length scales. One of the fundamental issues that arise concerns the choice of the most suitable u and ℓ scales to model the interface deformation. For flows over a flat plate [10, 11] and channel flows [13], friction-based variables were used. Furthermore, in these works, the contact line was assumed to be pinned on the roughness elements edges, implying that the characteristic length scale of the interface deformation is the typical texture size. Conversely, [9] used a pressure-based velocity since the bluff-body wake was predominated by a massive separation. In addition, interface deformation much larger than the roughness size was reported. Rather than the texture size, the sphere diameter d was chosen as scaling parameter. However, these results were obtained in the so-called terminal conditions, which might not reflect the early stage of interactions between the flow and the deforming interface. This lack of a comprehensive understanding has motivated the present study, which aims to bring a better insight on the role of the interface deformation on the performance of SH surfaces. Doing so, we attempt to bridge the results reported in [10, 11, 13] with those of [9]. To address this issue, we investigate the onset of transition in the wake of a canonical bluff-body, i.e. a falling sphere, in presence of SH coatings. A large number of studies (see e.g. the review by [14]) investigated the role of parameters as body shape and boundary condition at the wall on the development of the wake of free falling/rising objects. Fewer works have been devoted to the analysis of SH falling spheres with a specific attention on the capability of the wall slippage to modify the terminal velocity u_∞ , and accordingly the terminal drag coefficient [9, 15, 16, 17, 18]. However, none of these studies were dedicated to the analysis of wake transition. This is the goal of this work, which aims to evidence a possible influence of SH coatings on the transition process and to identify the

relevant scales to be used for modelling the role of interface deformation.

The paper is organised as follows: the experimental set-up is described first, followed by a characterisation of the manufactured SH coatings. After a brief comparison with previous studies, results sampled from the executed experimental campaign are presented. Finally, the article is completed by an overall discussion and overview of the evidenced phenomena.

2. Experimental set-up

2.1. The falling sphere facility

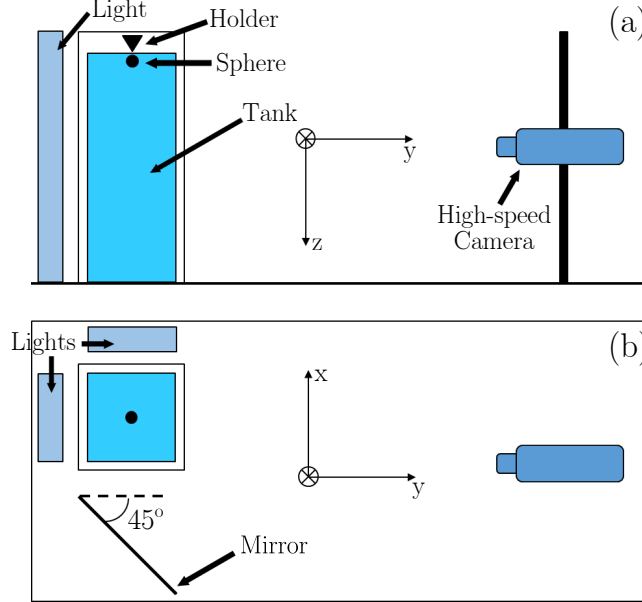


Figure 1: Schematic of the falling sphere experimental set-up. (a), side view. (b) top view.

Experiments were carried out using the same set-up as the one described in [9], therefore its main characteristics are only briefly recalled hereinafter. The falling sphere experiments were performed in a transparent vertical tank with a $100 \times 100 \text{ mm}^2$ square cross-section and a 650 mm height (see Fig. 1).

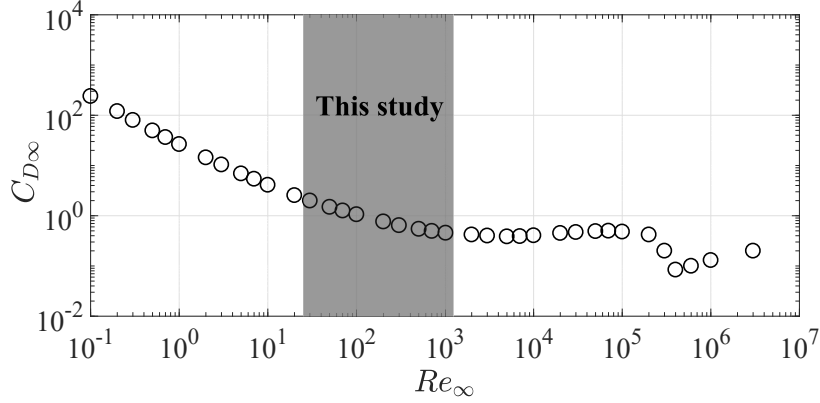


Figure 2: Terminal drag coefficient $C_{D\infty}$ as a function of the terminal Reynolds number Re_{∞} for reference spheres. \circ , experimental data from [19]. The gray rectangle indicates the Re_{∞} range under investigation in this study, which focuses on the influence of wall properties on the onset of wake transition.

All tests were performed at room temperature equal to 20 ± 1 °C, which was monitored by a thermocouple dipped in the liquid filling the tank. At the beginning of the test, the spheres were gently dipped below the liquid free surface by an electromagnetic holder. The latter was then used to control the release of the sphere, thus assuring a null initial velocity. In this study, glycerine-water mixtures are used as working fluids. As emphasized in Fig. 2 which reports the well-known evolution of the terminal drag coefficient $C_{D\infty} (\equiv 8D/(\pi\rho u_{\infty}^2 d^2))$ with D the drag, ρ the liquid density, u_{∞} the terminal velocity and d the sphere diameter) with respect to the terminal Reynolds number $Re_{\infty} (\equiv u_{\infty} d/\nu$ with ν the liquid kinematic viscosity), a broad range of operating conditions can be spanned by varying both the volumetric fractions of the two liquids in the mixtures (see Tab. 1) and the sphere diameter. In this study, Re_{∞} ranges from 2.5×10^1 to 1.0×10^3 , which covers the wake transition regime of falling spheres [14]. It is worth noting that for each operating condition, 10 tries have been performed to assess statistical convergence. The settling time between two successive tries has been set to 30 min, which has been found to be enough to assure the liquid to be quiescent for each experiment.

Mixture Name	Water Fraction, [%]	Glycerine Fraction, [%]	Diameter Range, [mm]
G060	40	60	5-10
G070	30	70	5-10
G080	20	80	5-10

Table 1: Nomenclature and properties of the glycerine-water mixtures investigated in the falling spheres experimental campaign. The water and glycerine percentages represent the volumetric fractions. The last column indicates the sphere diameter range investigated in each mixture.

The trajectory of the falling sphere was recorded by a Phantom V341 high-speed camera and the configuration resulted into a spatial resolution of 0.3 mm px^{-1} . The recording frame rate varied in the range $700 - 1000 \text{ fps}$ since it was adapted to the falling sphere velocity magnitude, which strongly varied depending on the operating conditions. The transversal motion in the $z-y$ plane was made available by the presence of a mirror placed at 45° with respect to the tank side wall. The three-dimensional (3D) time-resolved displacement of the sphere was reconstructed by a cross-correlation code developed in MATLAB[®]. A sub-pixel accuracy of $\approx \pm 0.06 \text{ px}$, that is lower than 0.4% of the smallest sphere diameter, was achieved by a Gaussian fit of the correlation peak [20]. In order to limit the experimental noise amplification, the velocity profiles were obtained via the smoothing spline technique described in [21]. When necessary, the velocities were corrected for confinement effects due to the finite size of the tank cross-section following the technique proposed by [22].

2.2. Coating properties

The SH spheres were produced by applying a SH coating over smooth stainless steel spheres via a spray method, using a commercially available SH painting (Ultra-Ever Dry[®]). The manufacturing procedure was explained in detail in [9].

It consists in spraying an etch primer to create a suitable substrate, eventually enhancing the surface roughness by embedding a carbon-based powder with the desired particle size d_p and finally spraying a top coating that assures the SH behaviour to be achieved. The coating without embedded powder as intermediate layer will be called SH-1. The two coatings with embedded powder will be indicated hereinafter as SH-2 ($d_p \approx 70 \mu m$) and SH-3 ($d_p \approx 200 \mu m$). Typical examples of the surface roughness reconstructed via 3D digital microscopy are shown in Fig. 3 for the three produced coatings. It clearly appears that the properties of surface roughness are strongly impacted by the powder inclusion. For instance, the maximum peak height increased from about $50 \mu m$ in the case of the SH-1 coating (Fig. 3(a)) up to around $370 \mu m$ for the SH-3 coating (Fig. 3(c)). In all cases, the manufactured coatings resulted into a random distribution of the surface roughness. A quantitative characterisation of the surface texture was obtained by evaluating the root-mean-square surface roughness:

$$\lambda = \sqrt{\frac{1}{N} \sum_{i=1}^N z_i^2}, \quad (1)$$

where z_i represents the local roughness height and N the total amount of pixels in the image. In practice, the 3D model in Fig. 3 was converted into the corresponding 2D wall-normal projected grayscale image, where each pixel stored information on the local z_i , thus enabling the λ estimation. As shown in Tab. 2, λ varies within the range $25 - 142 \mu m$.

Besides, Tab. 2 emphasizes the slippage capability of the SH surfaces against pure water (i.e. G000) and pure glycerine (i.e. G100). To this end, both static contact angles ϑ_s and hysteresis angles ϑ_h have been estimated via a sessile drop technique with a digital goniometer over SH flat plates. It can be noted that each SH surface is characterized by a large static contact angle and a small hysteresis angle, thus highlighting their ability to repel each of the liquids used in the mixtures. However, a slight degradation in performance can be seen when the roughness increases, which agrees with the trend reported by [23]. Finally,

		SH-1	SH-2	SH-3
	$\lambda, [\mu m]$	25 ± 4	74 ± 12	142 ± 23
G000	$\vartheta_s, [\text{deg.}]$	160.7 ± 2.8	150.1 ± 3.0	145.7 ± 2.0
	$\vartheta_h, [\text{deg.}]$	2.3 ± 0.5	4.3 ± 2.0	11.9 ± 3.6
	$\vartheta_s, [\text{deg.}]$	156.4 ± 5.8	147.3 ± 7.6	136.7 ± 12.0
G100	$\vartheta_h, [\text{deg.}]$	2.7 ± 0.7	4.1 ± 2.3	13.2 ± 4.7

Table 2: Properties of the manufactured SH coatings. λ , root-mean-square surface roughness (see Eq. (1)). ϑ_s , static contact angle. ϑ_h , hysteresis angle. The reported uncertainties represent the 95% confidence level. The ϑ_s and ϑ_h values are shown for the two extreme cases of pure water (G000) and pure glycerine (G100).

the slippage capability seems to be very weakly dependent on the tested liquid.

2.3. Comparison with previous studies

It is worth comparing the set of operating conditions achieved in this work to those reported in previous studies. Since in the investigated regime (see Fig. 2) the wake is induced by a massive separation, one can assume that the viscous drag accounts for about 10% of the total drag. This yields $u_\tau/u_\infty = O(10^{-1})$, where u_τ is the friction velocity. In this study, the typical texture size expressed in wall units, $\lambda^+ \equiv \lambda u_\tau/\nu$, remains lower than unity, which is much smaller than the critical value beyond which plastron depletion could occur [10, 11]. This means that our experiments are not expected to be influenced by the transition from the Cassie-Baxter state (dewetted roughness) to the Wenzel state (roughness infused by the liquid). This was confirmed by a close examination immediately after each experiment to verify that the coated spheres were dry when removed from the tank. The friction-based Weber number, $We^+ = \rho u_\tau \nu / \gamma$, lays within the range $2 \times 10^{-2} - 2 \times 10^{-1}$, which is noticeably larger than those used in [10, 11, 13]. It is also worth noting that the We^+ range covered here is at least 3 orders of magnitude larger than the value estimated

from the data reported by [6]. Overall, this indicates that in our experiments, the operating conditions are likely to promote the deformation of the interface. Finally, the diameter-based Weber number $We_d = \rho u_\infty^2 d / \gamma$ is within the range covered in [9].

3. Results

An indication of the Re_∞ reached in this study is reported in Tab. 3. These data show that, varying the fractions of the two liquids and the sphere diameter, the ranges achieved with the different mixtures overlap. This choice was made to cover the Re_∞ regions where the sphere wake transition occurs [24]. In fact, in the case of a fixed sphere, the axisymmetric wake characterising the low Re_∞ region is lost at $Re_\infty = Re_{cr,1} \approx 212$ in favour of a steady planar-symmetric wake. The latter becomes periodic at $Re_\infty \approx 275$, while losing the symmetry for $Re_\infty \geq 350$. A further Re_∞ increase leads to the so-called *chaotic* regime, where the detection of an unambiguous frequency of the vortex shedding is no more easily feasible. The transition mechanism was shown to keep qualitatively similar in the case of a free falling/rising sphere, highlighting the close relationship between wake and path instability [14]. Moreover, the critical Reynolds number at which path instability of a free body and wake instability of a fixed sphere occur were shown to be closely related. This comparison is even more relevant as far as the density ratio ζ between the solid and the liquid increases. It is worth noting that in this study, $\zeta > 5$, for which [24] reported only marginal departure from the case of a fixed sphere.

In the following, the survey of transversal motion is used to assess the onset of wake instability. Indeed, reflectional symmetry breaking induced by the first wake transition at the critical Reynolds number $Re_{cr,1}$ yields a lift force resulting in a departure from the original vertical falling trajectory. In this study, the transversal velocity $u_{tr} = \sqrt{u_x^2 + u_y^2}$ (u_x and u_y being the velocity components in the x – y plane as shown in Fig. 1) is used as a metric to quantify the amplitude of the transversal motion. Fig. 4 displays the evolution of the normalised transversal velocity $u_{tr}^* = u_{tr}/u_0$ of the $d = 10$ mm spheres for the mixture G080

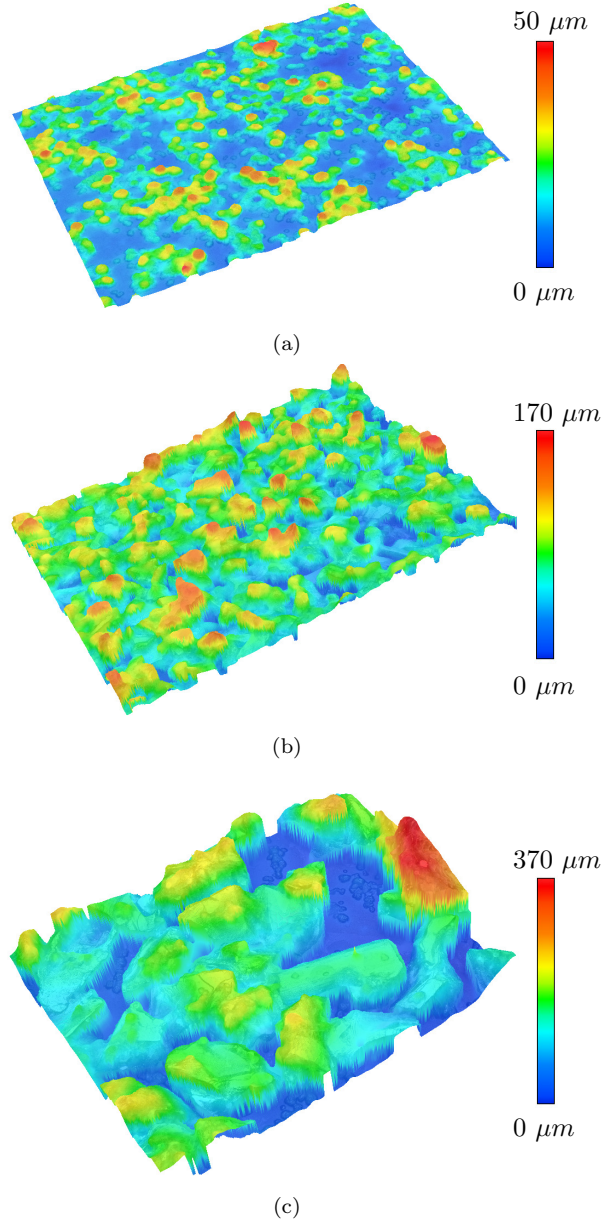


Figure 3: 3D Digital microscopy analysis of a portion ($1.5 \times 1.0 \text{ mm}^2$) of a flat plate covered with a SH coating. (a), SH-1. (b), SH-2. (c), SH-3. The color scales indicate the range of surface roughness per each coating.

and of the $d = 5 \text{ mm}$ spheres for the mixture G070, both reaching $Re_\infty \approx 100$ (see Tab. 3). The time $t_0 = \sqrt{d/((\zeta - 1)g)}$ where g is the acceleration due to gravity and the velocity $u_0 = \sqrt{(\zeta - 1)gd}$ were chosen as scaling parameters to take into account gravity/buoyancy effects [24]. For what concerns the reference spheres, since $Re_\infty < Re_{cr,1}$, the wake is expected to be axisymmetric, which is well supported by the experimental results exhibiting a marginal transverse motion. For the SH spheres, although the transversal velocity remains very small in comparison with its vertical counterpart (one order of magnitude of difference), one can clearly see the onset of transversal motion as revealed by the appearance of a sudden u_{tr}^* increase. This transversal motion is further enhanced as far as surface roughness is increased. Then, u_{tr}^* falls down until it almost collapses on the reference case values, meaning that the promoted instability is damped. This promotion-damping phenomenon caused by the SH coatings on the transversal motion suggests that the Reynolds number alone might not be enough to fully describe the transition mechanism. An additional suitable parameter should be sought.

As evidenced in Fig. 5, this scenario is confirmed when investigating the transversal velocity profiles obtained for Re_∞ lying within the wake transition regimes (red color in Tab. 3). Interestingly, it appears that the wake instability is triggered earlier for SH surfaces compared to reference no-slip walls. This effect is further enhanced when the dimensionless surface roughness λ/d

$d, [mm]$	G080	G070	G060
5	25	100	290
8	65	250	680
10	110	390	1030

Table 3: Averaged terminal Reynolds number Re_∞ achieved in this study. The text colors discriminate between the Re_∞ values below (blue) and above (red) the first transition region reported for the fixed sphere case ($Re_{cr,1} \approx 212$) [14].

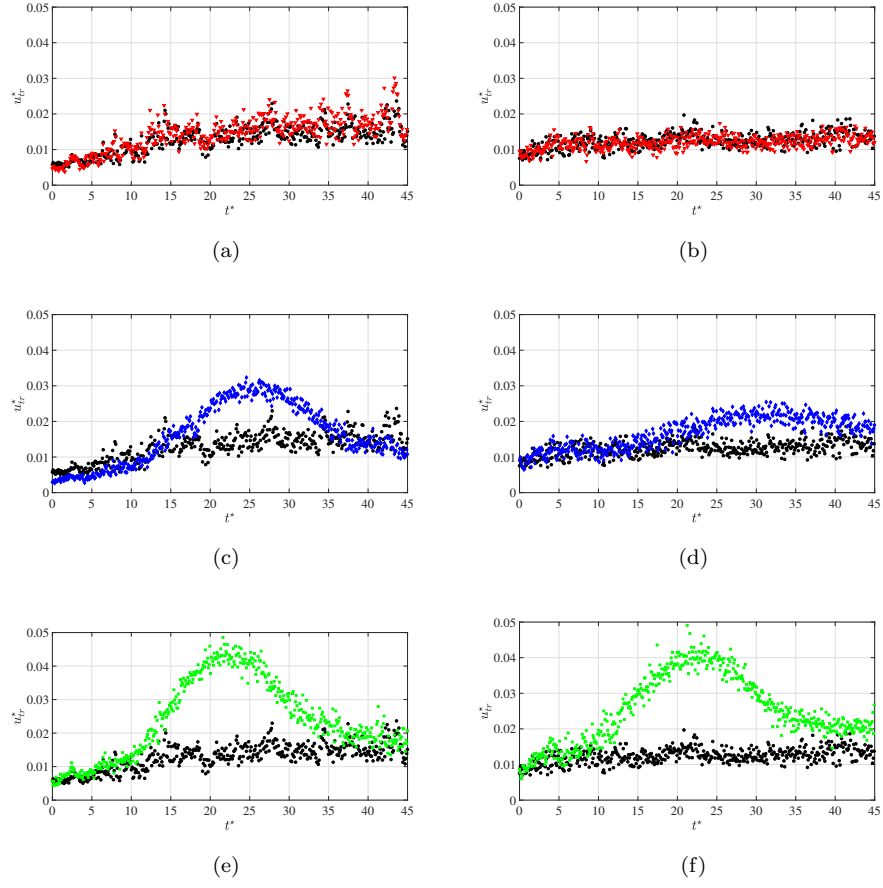


Figure 4: Time history of dimensionless transversal velocity u_{tr}^* for (left) $Re_\infty = 110$ ($d = 10$ mm - mixture G080) and (right) $Re_\infty = 100$ ($d = 5$ mm - mixture G070). The normalized surface roughness λ/d increases from top to bottom. \bullet , reference. \blacktriangledown , SH-1. \blacklozenge , SH-2. \blacksquare , SH-3.

is increased. However, at terminal conditions, the magnitude of the transversal motion of both reference and SH surfaces seems to converge towards each other. This behavior is corroborated by the drag coefficient values at terminal conditions, which is found to be weakly sensitive to the surface properties, and is thus not reported here. Indeed, it has been observed that the $C_{D\infty}$ variations were limited in the range $\pm 5\%$ for the SH coatings with respect to the corresponding reference sphere.

To go one step further, we introduce the normalized critical vertical velocity $u_{z,cr}^*$, which is estimated as schematically displayed in Fig. 6. A threshold transversal velocity value \bar{u}_{tr}^* is set, thus allowing to identify a critical time t_{cr}^* of the onset of transversal motion. The choice of the threshold transversal velocity value $\bar{u}_{tr}^* = 0.05$ was based on the maximum value of the u_{tr}^* peak identified in Fig. 4, which corresponds to the case of weak if not negligible transversal motion. Moreover, by looking at the u_{tr}^* profiles in Fig. 5 where transversal motion is significant, the chosen threshold is sufficiently high to be above the u_{tr}^* values at the beginning of the drop ($t^* < 10$). This assures a meaningful detection of the critical time values, which otherwise could be excessively biased by too large uncertainties in the point detection. In conjunction with the vertical velocity history, the t_{cr}^* value can then be used to estimate the critical vertical velocity value $u_{z,cr}^*$ where wake instability is triggered.

Accordingly, the critical Reynolds number can be defined as $Re_{cr} = u_{z,cr}^* Re_0$ with $Re_0 = u_0 d / \nu$. The effect of surface properties on wake stability can then be estimated by introducing the critical Reynolds number variation $\Delta Re_{cr} = Re_{cr}^{SH} / Re_{cr}^{ref} - 1$, which takes positive values if transition is delayed and negative values otherwise. As emphasized in Fig. 7, the onset of wake transition of SH spheres appears at lower critical Reynolds numbers compared to the reference case. This trend is made evident increasing the surface roughness. This result disagrees with those reported by [4] who observed a wake transition delay and drag mitigation when introducing slip on the wall of a circular cylinder at low Reynolds number. However, since 3D wake transition behaves differently from 2D and axisymmetric bluff-body geometries [see e.g., 25], the comparison with

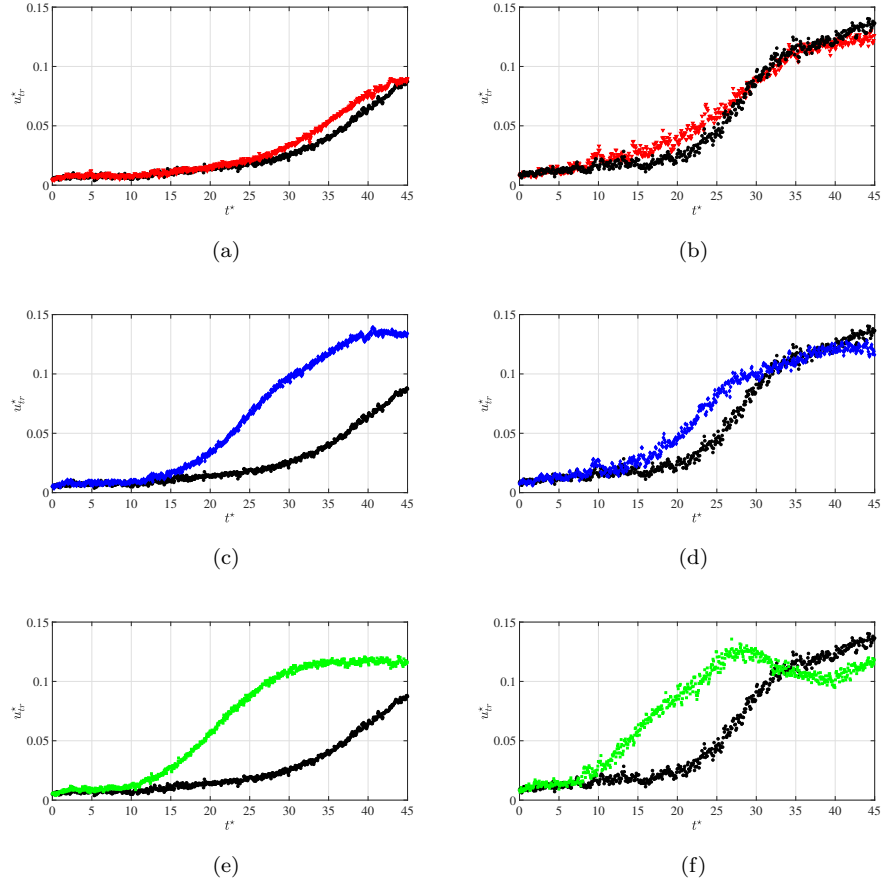


Figure 5: Time history of dimensionless transversal velocity u_{tr}^* for (left) $Re_\infty = 250$ ($d = 8$ mm - mixture G070) and (right) $Re_\infty = 290$ ($d = 5$ mm - mixture G060). The normalized surface roughness λ/d increases from top to bottom. \bullet , reference. \blacktriangledown , SH-1. \blacklozenge , SH-2. \blacksquare , SH-3.

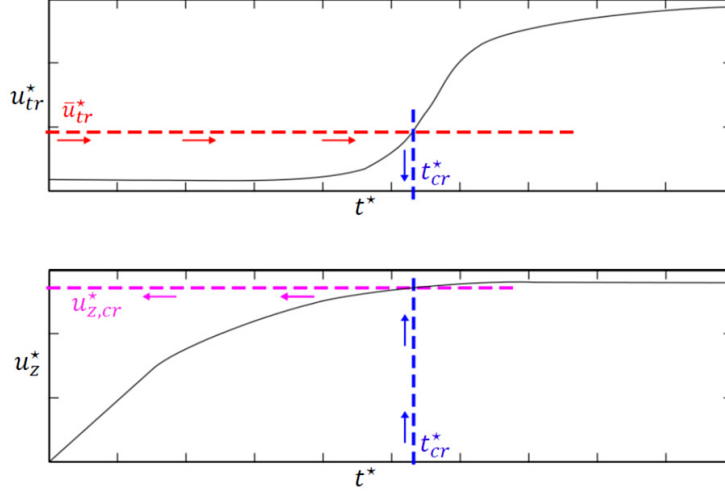


Figure 6: Schematic of the approach implemented to identify the vertical velocity value at critical conditions $u_{z,cr}^*$. A threshold \bar{u}_{tr}^* is imposed on the transversal velocity profile u_{tr}^* (upper plot), thus identifying the corresponding critical time t_{cr}^* . The latter is then used to enter the u_z^* chart (lower plot). The coloured arrows indicate the logical path direction.

[4] should be made with caution. Nevertheless, it is worth noting that their numerical simulations were based on a ideal representation of the boundary condition, which was assumed to be undeformable.

4. Discussion and concluding remarks

An attempt to explain the behaviour we observed is made by taking a closer look to the phenomena occurring in the near-wall region. As a matter of example, a sequence of images taken during the drop of a $d = 10 \text{ mm}$, SH-3 sphere in the G070 mixture is shown in Fig. 8. These images clearly show that the air layer initially trapped among the roughness elements tends to interact with the flow around the falling object, by deforming and moving around the rear-side of the sphere. In fact, while no significant deformation is detectable in Fig. 8(a), the macroscopic deformed air pocket is clearly visible in both Figs. 8(b) and 8(c), while in Fig. 8(d) it turned towards the non-visible region of the sphere and shifted even more in the rear-side of the sphere. This scenario thus suggests

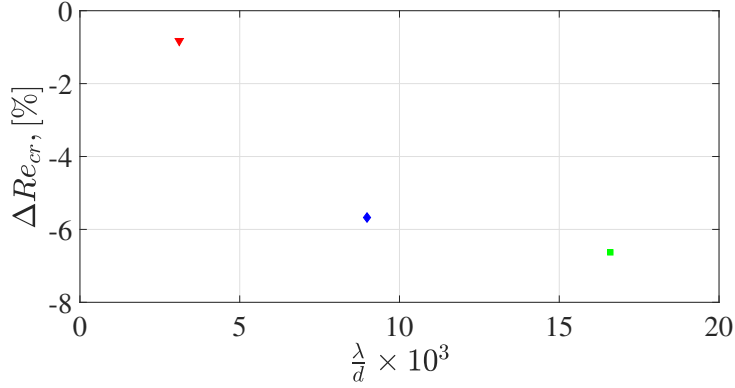


Figure 7: Variation of the critical Reynolds number of SH coatings with respect to the reference ($Re_\infty \approx 250$ - $d = 8$ mm - mixture G070) as a function of the non-dimensional surface roughness λ/d . ▼, SH-1. ♦, SH-2. ■, SH-3.

an interconnection between the flow developing around the falling sphere and the air layer behaviour.

In fact, the deformed air pocket is detected only in the rear-side of the falling sphere, that is the region where the laminar boundary layer underwent separation and transition to turbulence [26]. As introduced in [9], we can thus speculate that the pressure jump due to flow separation could promote the partial suction of the air layer initially trapped among the roughness elements, with a possible feedback influence on the wake development and therefore on the onset of the transversal motion. In a sense, this mechanism is qualitatively comparable to that reported by [27] who studied the transition induced by a smooth bump immersed within a laminar boundary layer. These authors observed that large amplification could be achieved combining high enough Reynolds number and roughness height. The latter is assimilated to the protuberance visible in Figs. 8(b) and 8(c). Even though this scenario is tempting, a direct comparison should be made with care, since in [27] the protrusion shape and position were steady.

Although the images displayed in Fig. 8 qualitatively resemble those reported in [9], they differ considerably from a quantitative point of view. Indeed,

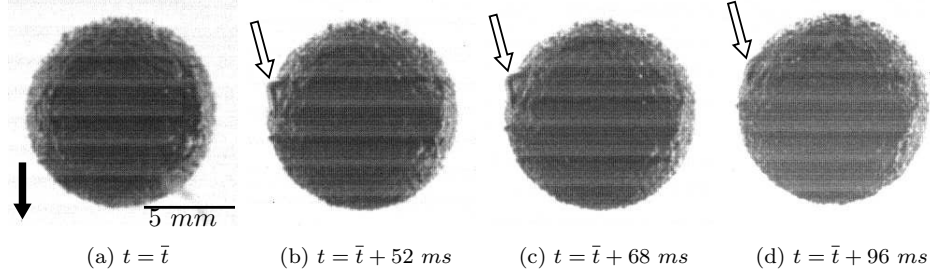


Figure 8: Frames sampled during the drop of a $d = 10 \text{ mm}$, SH-3 sphere in the G070 mixture illustrating the motion and the deformation of the air layer (indicated by white arrows). The black arrow represents the gravity direction. The variable \bar{t} designates a randomly chosen time origin.

while deformations that can reach sizes of the order of magnitude of d have been observed in [9], here the protuberances are much smaller than d . This implies that the sphere diameter is no more a relevant parameter to characterize the early stage of the interaction between the flow and the deforming interface. In other words, the diameter-based Weber number appears to be unsuited to faithfully describe the onset of wake instability. To address this issue, let us carry out a simple scaling analysis of the linearised Young-Laplace equation $\nabla^2 \eta = \Delta P / \gamma$, where η and ΔP denote the interface deformation and the pressure difference across the interface, respectively. Following the work of [10, 11, 13], we first assume that the early stage of the air plastron deformation is intimately connected to the surface roughness λ (this is well supported by the fact that the typical length scale of the protuberance in Figs. 8(b) and 8(c) is of the same order of magnitude than λ). In addition, we assume that the separation-induced suction is the driving mechanism of the interface deformation. It then comes $\eta / \lambda \sim \rho u_0^2 \lambda / \gamma$, which suggests that the deformation relative to the typical roughness size could be governed by a roughness-based Weber number such that $We_\lambda = \rho u_0^2 \lambda / \gamma$, which reflects the relative competition between hydrodynamic and capillary effects. Notice that the condition $We_\lambda \rightarrow 0$ is equivalent to the non-deformable interface assumption, while the air-liquid

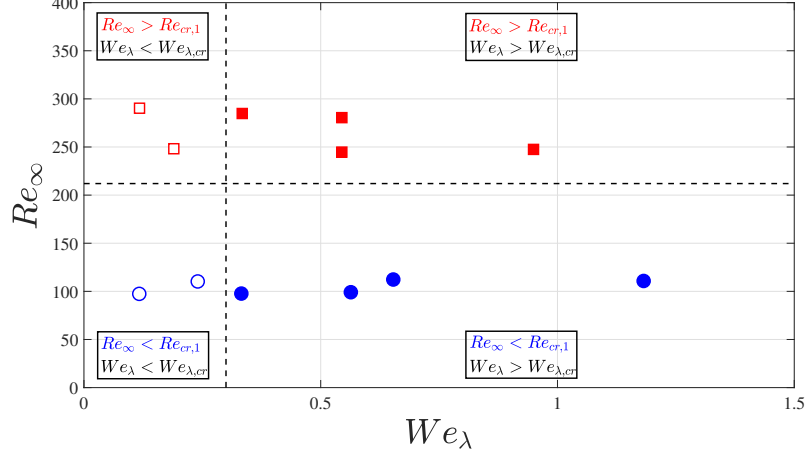


Figure 9: Diagram of hydrodynamic-deformation interactions summarizing the results reported in Fig. 4 (blue circles) and Fig. 5 (red squares). Empty symbols denote no significant difference with respect to no-slip wall conditions (i.e., reference spheres), while full symbols indicate a noticeable effect of the SH surface. The horizontal dashed line represents the critical Reynolds number $Re_{cr,1}$, while the vertical dashed line symbolises the critical Weber number $We_{\lambda,cr}$.

interface becomes more prone to deformation as far as We_λ increases. It should be noted that the interface deformation is expected to scale with We_λ insofar as the contact line remains pinned to the edges of the roughness. However, once this condition is released, the flow/interface interaction could be governed by the diameter-based Weber number We_d as proposed in [9]. This change in behaviour may require a certain amount of hydrodynamic energy, which could be achievable only for large enough Reynolds number.

The results displayed in Figs. 4 and 5 can be summed up within a single $Re_\infty - We_\lambda$ chart, as shown in Fig. 9. This diagram emphasises the possible interactions between the hydrodynamic disturbances, scaling with the Reynolds number, and the interface deformation, scaling with the Weber number. Interestingly, it is found that the effectiveness of SH surfaces to modify the transition behavior depends not only on the critical Reynolds number $Re_{cr,1}$ but also on a critical Weber number, whose value, under the operating conditions of this

study, was found to be $We_{\lambda,cr} \approx 0.3$. Accordingly, the disturbance-deformation interactions could be decomposed within 4 regions, which are sketched in Fig. 10 in comparison to the no-slip wall case (see Figs. 10(a) and 10(b)). For $We_{\lambda} < We_{\lambda,cr}$ (see Figs. 10(c) and 10(d)), negligible impact of the SH coating on the wake dynamics is observed for both $Re_{\infty} < Re_{cr,1}$ and $Re_{\infty} > Re_{cr,1}$ (empty symbols in Fig. 9). This means that capillary effects predominate over the inertial counterpart, thus implying that the interface is weakly receptive to hydrodynamic perturbations. In this regime, for what concerns wake transition, the SH surfaces behave like the reference one. These conditions are met in Figs. 4(a), 4(b) and Figs. 5(a), 5(b), respectively. A scenario where instabilities are first promoted and then damped characterises the region where $We_{\lambda} > We_{\lambda,cr}$ and $Re_{\infty} < Re_{cr,1}$ (lower-right region in Fig. 9). In this regime, the interface has the capability to deform (see Fig. 10(e)), triggering thereby instabilities. However, this deformation might induce an energy dissipation excess of the surrounding flow, which in turns could lead to a damping of the instabilities since the baseline hydrodynamic disturbances are not strong enough to counterbalance the energy loss. This case corresponds to Figs. 4(c), 4(d), 4(e) and 4(f). It suggests that the flow should contain a *minimum seeding* of disturbances for activating the feedback mechanism. This condition could be met only for high enough Reynolds number, i.e. $Re_{\infty} > Re_{cr,1}$, and for highly receptive interface, i.e. $We_{\lambda} > We_{\lambda,cr}$ (upper-right region in Fig. 9). This corresponds to the last regime depicted in Fig. 10(f) where the interface deformation may act as a by-pass mechanism yielding an earlier transition. Notice that the interface deformation still leads to an extra-consumption of energy for the flow, which may explain that while transition is triggered earlier the feedback mechanism does not imply instability amplification, at least in the operating conditions covered in this study. This scenario is representative of the results reported in Figs. 5(c), 5(d), 5(e) and 5(f) where the onset of significant transversal motion is detected earlier for SH spheres, but u_{tr}^* tends towards similar values with respect to the reference when approaching terminal conditions.

Finally, altogether our results suggest that interface deformation is a key

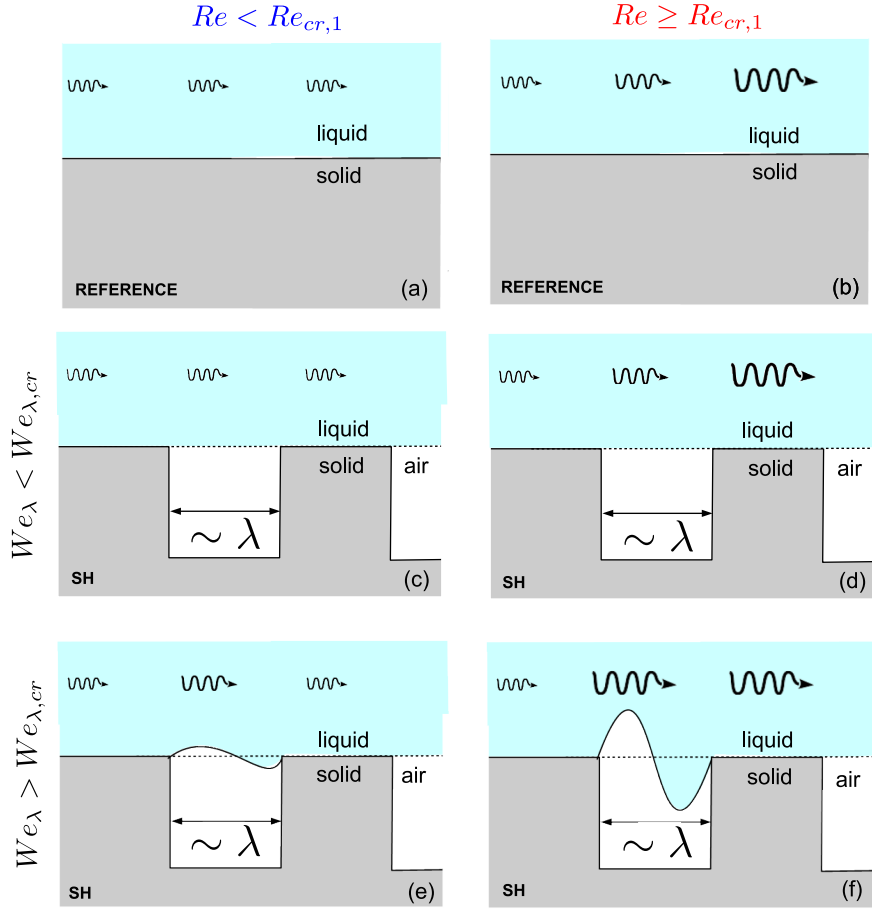


Figure 10: Conceptual scenario of the transition mechanisms over no-slip walls (a, b) and SH walls (c to f). The undulated arrows represent the hydrodynamic perturbations, which are amplified during transition phase (right side, above the critical Reynolds number $Re_{cr,1}$). For SH surfaces, the interface deformation scales with the roughness-based Weber number We_λ with the threshold represented by the critical value $We_{\lambda,cr}$.

mechanism for the development of the wake of SH spheres. Unlike what has been predicted from numerical simulations based on ideal boundary conditions, it has been evidenced that slippery wall might trigger wake transition earlier than no-slip wall. The survey of the $Re_\infty - We_\lambda$ parametric space emphasised different interaction regimes, which are delimited by the critical Reynolds number $Re_{cr,1}$ and a critical Weber number $We_{\lambda,cr}$. For what concerns wake instabilities, the SH surfaces may behave as no-slip walls or trigger early transition depending on the operating conditions. Although these results bring new insights about the physics underlying SH bluff-bodies, which is of primary interest for the design of effective coatings in practical applications, the extrapolation to other flow conditions and body geometries should be made with caution. For instance, baseline transition could differ in presence of free-stream turbulence, which was not taken into account in this study. This implies that the achievement of a comprehensive understanding of the behaviour of SH surfaces requires further studies, which should consider the air-liquid interface deformation as one of the parameters possibly influencing the hydrodynamic performance. Such sophisticated models will be obtained by incorporating challenging issues such as the contact line dynamics, which is fundamental to bridge the early stage of interaction with the fully coupled regime.

Acknowledgments

This work was supported by the Direction Générale de l’Armement (DGA), Ministère de la Défense, République Française and the Agence Nationale de la Recherche (ANR) through the Investissements d’Avenir Program under the Labex CAPRYSES Project (ANR-11-LABX-0006-01).

References

- [1] X. Zhang, F. Shi, J. Niu, Y. Jiang, Z. Wang, Superhydrophobic surfaces: from structural control to functional application, *J. Mater. Chem.* 18 (2008) 621–633.

- [2] T. Min, J. Kim, Effects of hydrophobic surface on stability and transition, *Phys. Fluids* 17 (10) (2005) 108106.
- [3] F. Picella, J.-C. Robinet, S. Cherubini, Laminar–turbulent transition in channel flow with superhydrophobic surfaces modelled as a partial slip wall, *J. Fluid Mech.* 881 (2019) 462–497.
- [4] D. Legendre, E. Lauga, J. Magnaudet, Influence of slip on the dynamics of two-dimensional wakes, *J. Fluid Mech.* 633 (2009) 437–447.
- [5] Y. Xiong, D. Yang, Influence of slip on the three-dimensional instability of flow past an elongated superhydrophobic bluff body, *J. Fluid Mech.* 814 (2017) 69–94.
- [6] P. Sooraj, M. S. Ramagya, M. H. Khan, A. Sharma, A. Agrawal, Effect of superhydrophobicity on the flow past a circular cylinder in various flow regimes, *J. Fluid Mech.* 897 (2020) A21.
- [7] D. Song, B. Song, H. Hu, X. Du, P. Du, C.-H. Choi, J. P. Rothstein, Effect of a surface tension gradient on the slip flow along a superhydrophobic air–water interface, *Phys. Rev. Fluids* 3 (2018) 033303.
- [8] J.-H. Kim, J. P. Rothstein, Role of interface shape on the laminar flow through an array of superhydrophobic pillars, *Microfluid. Nanofluid.* 21:78 (2017) 1–12.
- [9] M. Castagna, N. Mazellier, A. Kourta, Wake of super-hydrophobic falling spheres: influence of the air layer deformation, *J. Fluid Mech.* 850 (2018) 646–673.
- [10] J. Seo, R. García-Mayoral, A. Mani, Pressure fluctuations and interfacial robustness in turbulent flows over superhydrophobic surfaces, *J. Fluid Mech.* 783 (2015) 448–473.
- [11] J. Seo, R. García-Mayoral, A. Mani, Turbulent flows over superhydrophobic surfaces: flow-induced capillary waves, and robustness of air–water interfaces, *J. Fluid Mech.* 835 (2018) 45–85.

- [12] E. J. G. Cartagena, I. Arenas, M. Bernardini, S. Leonardi, Dependence of the drag over super hydrophobic and liquid infused surfaces on the textured surface and weber number, *Flow Turbul. Combust.* 100 (2018) 945–960.
- [13] F. Picella, J.-C. Robinet, S. Cherubini, On the influence of the modelling of superhydrophobic surfaces on laminar–turbulent transition, *J. Fluid Mech.* 901 (2020) A15. doi:10.1017/jfm.2020.516.
- [14] P. Ern, F. Risso, D. Fabre, J. Magnaudet, Wake-induced oscillatory paths of bodies freely rising or falling in fluids, *Annu. Rev. Fluid Mech.* 44 (2012) 97–121.
- [15] G. McHale, N. J. Shirtcliffe, C. R. Evans, M. I. Newton, Terminal velocity and drag reduction measurements on superhydrophobic spheres, *Appl. Phys. Lett.* 94 (2009) 064104.
- [16] C. Byon, Y. Nam, S. J. Kim, Y. S. Ju, Drag reduction in stokes flows over spheres with nanostructured superhydrophilic surfaces, *J. Appl. Phys.* 107 (2010) 066102.
- [17] I. U. Vakarelski, D. Y. C. Chan, S. T. Thoroddsen, Leidenfrost vapour layer moderation of the drag crisis and trajectories of superhydrophobic and hydrophilic spheres falling in water, *Soft Matter* 10 (31) (2014) 5662–5668.
- [18] K. M. T. Ahmmed, C. Patience, A.-M. Kietzig, Internal and external flow over laser-textured superhydrophobic polytetrafluoroethylene (PTFE), *ACS Appl. Mater. Interfaces* 8 (2016) 27411–27419.
- [19] C. E. Lapple, C. B. Sheperd, Calculation of particle trajectories, *Ind. Eng. Chem.* 32 (1940) 605–617.
- [20] M. Raffel, C. Willert, S. Wereley, J. Kompenhans, *Particle Image Velocimetry*, Springer, 2007.

- [21] B. Epps, T. T. Truscott, Evaluating derivatives of experimental data using smoothing splines, *Mathematical Methods in Engineering International Symposium, IPC, Coimbra, Portugal* (2010) 29–38.
- [22] R. Di Felice, A relationship for the wall effect on the settling velocity of a sphere at any flow regime, *Int. J. Multiphase Flow* 22 (3) (1996) 527–533.
- [23] M. A. Nilsson, R. J. Daniello, J. P. Rothstein, A novel and inexpensive technique for creating superhydrophobic surfaces using teflon and sandpaper, *J. Phys. D: Appl. Phys.* 43 (4) (2010) 045301.
- [24] M. Jenny, J. Dušek, G. Bouchet, Instabilities and transition of a sphere falling or ascending freely in a Newtonian fluid, *J. Fluid Mech.* 508 (2004) 201–239.
- [25] G. J. Sheard, M. C. Thompson, K. Hourigan, From spheres to circular cylinders: the stability and flow structures of bluff ring wakes, *J. Fluid Mech.* 492 (2003) 147–180.
- [26] S. Taneda, Experimental investigation of the wake behind a sphere at very low Reynolds number, *J. Phys. Soc. Japan* 11 (10) (1956) 1104–1108.
- [27] S. Cherubini, M. De Tullio, P. De Palma, G. Pascazio, Transient growth in the flow past a three-dimensional smooth roughness element, *J. Fluid Mech.* 724 (2013) 642–670.